Drop fragmentation on impact

E. VILLERMAUX† AND B. BOSSA

IRPHE, Aix-Marseille Université, 13384 Marseille CEDEX 13, France

We address the sequence of events accompanying the transition from an initially compact volume of liquid – a drop – into dispersed fragments when it impacts a solid surface. We describe the change of topology of the drop to a radially expanding sheet and discuss the reasons of its rim destabilization, responsible for the emergence of radial ligaments which ultimately fragment into smaller drops. The dynamics ruling the radius of the sheet, its stability and the resulting fragment drop size distribution are documented experimentally. The radius dynamics results from a simple balance between inertia of the initial drop and capillary restoring forces at the rim, with damping due to the continuous transfer of momentum from the sheet to the rim. The ligaments expelled from the rim originate from a Rayleigh–Taylor mechanism localized at the rim. The final drop size distribution in the spray is shown to be a linear superposition of gamma distributions characteristic of ligament breakup, leading generically to Bessel functions.

Key words: aerosols/atomization, instability

1. Introduction

The change of topology of an initially compact liquid volume into a set of ligamentary structures, mandatory for subsequent breakup into smaller drops, is often enforced by an impact, either with a directed source of momentum or with a solid surface. Indeed, an obvious manifestation following the splash of a drop on a solid surface, on a thin layer of the same (Worthington 1908) or a different liquid (Thoroddsen, Etoh & Takehara 2006), is the formation of fingers and the eventual breakup of ligaments into drops. Since da Vinci contemplated the imprint of a drop crushed on a sheet of paper, the phenomenon has been a continuous source of amazement, ever renewed by the technological progress allowing it to be imaged (figure 1).

Most of the attention has however been devoted to describe the kinematics of the drop spreading as it flattens, its maximal radial extension and the number of fingers emerging from the resulting celebrated Worthington–Edgerton crown (Yarin 2006). Data on the fragmentation following the binary collision of drops, or their impact on a solid, are nevertheless scarce, and this is in spite of the relevance of the phenomenon to many natural and industrial processes (Villermaux 2007), some of which occurring at the scale of miniaturized ink jet printers up to that of the solar system (Stern *et al.* 2006).

† Also at Institut Universitaire de France, 75005 Paris, France. Email address for correspondence: villermaux@irphe. univ-mrs.fr
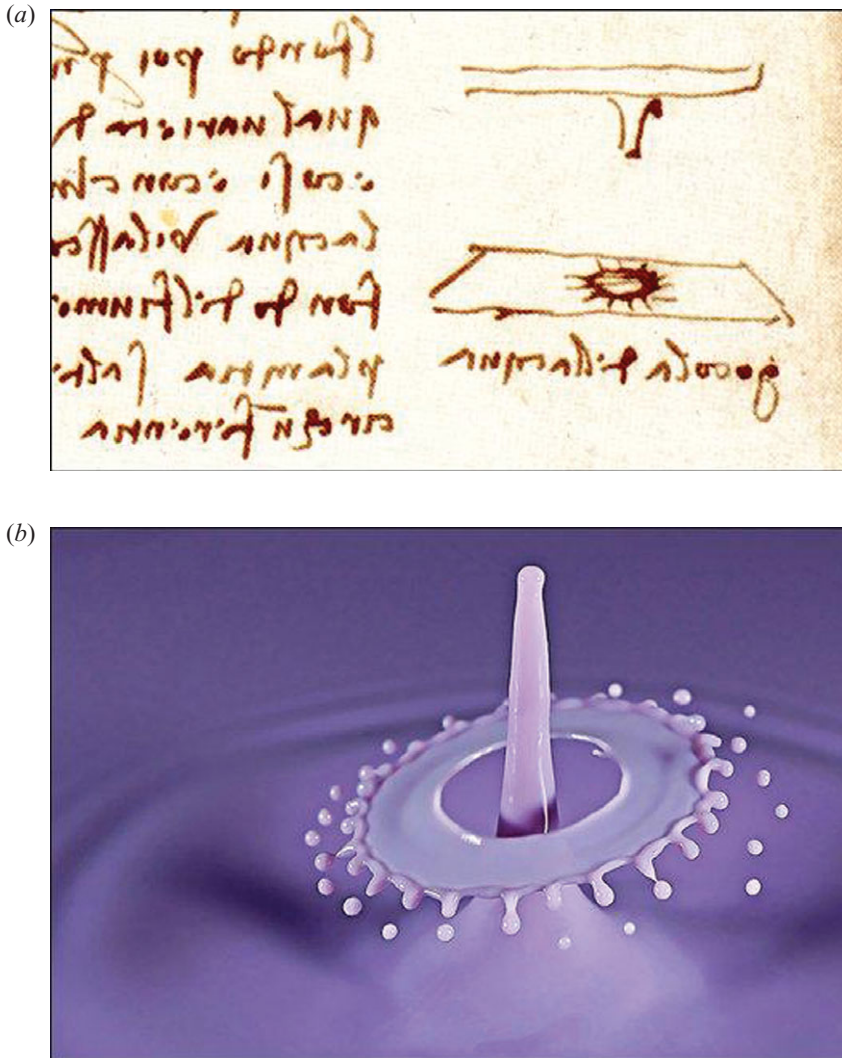
(*a*)

(*b*)

FIGURE 1. (Colour online) (*a*) Crushing of a water drop falling on a flat dense substrate. Drawing in the margin of *folio 33r* in the Codex Hammer (previously Codex Leicester, 1506–1510) by Leonardo da Vinci (1508) who notes there the axisymmetry of the impacted drop imprint pattern. Radial fingers are also visible. (*b*) A dramatic and neat illustration of the phenomenon discussed in the present paper: a train of drops drip into a glass of milkshake; a drop 'impales' on the jet emerging from the collapsing cavity formed by the previous drop. The expanding liquid sheet and rim drops are clearly visible. © Irene Müller (2006, http://www.pbase.com/daria90), by kind permission.

Among the relevant studies documenting fragmentation on impact are those of the following: Ashgriz & Poo (1990) and Qian & Law (1997), who quantified the conditions for coalescence or satellite formation in binary collisions of drops; Stow & Stainer (1977), who measured the number of fragments of a water drop colliding with various solid surfaces, dry, wet, smooth and rough, and measured their size distribution; Mundo, Sommerfeld & Tropea (1995), who performed similar measurements with liquids of different surface tension and viscosity; Yarin & Weiss (1995), who measured the fragment size distributions of a drop impacting a shallow

layer of the same fluid; Roisman, Horvat & Tropea (2006), who made various measurements on the spray resulting from an impact on a dry solid; and Xu, Barcos & Nagel (2007), who singled out the importance of the solid surface texture and ambient gas conditions on splashing and the resulting fragments' distribution. As for all fragmentation processes, a broad collection of fragment sizes is produced following drop impact, with a typical positively skewed size distribution presenting many small drops and few larger drops. The status of this distribution however remains obscure, and in spite of these notable progresses, the remark made by Stow & Stainer (1977, p. 518) more than 30 years ago is thus still largely topical:

> Almost without exception, recent investigations of splashing have concentrated on the observation of the hydrodynamics of the impact itself with little or no attention being paid to the final consequences of the event.

We may add that it is also conversely true that investigations documenting the 'final consequences of the event', namely the atomized products, usually pay little attention to the hydrodynamics of the initial deformation of the drop itself, nevertheless obviously responsible for the ultimate fragmentation process. The present paper is an attempt to establish this lacking link between the deterministic fluid mechanics and the statistical facets of the fragmentation process, a question ubiquitous in nature, far beyond the context of impacts.

We thus address here the complete sequence of events accompanying the transition from an initially compact drop into dispersed fragments when it impacts a solid target matching its own size, a configuration pioneered by Rozhkov, Prunet-Foch & Vignes-Adler (2002, 2003, 2004). We describe the change of topology of the drop to a radially expanding sheet (§3), and having understood its kinematics, we speculate on the reasons of its rim destabilization (§4), from which radial ligaments emerge. These ligaments ultimately fragment into smaller drops distributed in size according to a well-defined distribution. The construction mechanism of the drop size distribution in the overall spray is established experimentally (§5).

2. Set-up and chronology

We let a water (density $\rho = 10^3\,\mathrm{kg\,m^{-3}}$, surface tension $\sigma = 70 \times 10^{-3}\,\mathrm{N\,m^{-1}}$, viscosity $\nu = 10^{-6}\,\mathrm{m^2\,s^{-1}}$) or ethanol (density $\rho = 810\,\mathrm{kg\,m^{-3}}$, surface tension $\sigma = 22 \times 10^{-3}\,\mathrm{N\,m^{-1}}$, viscosity $\nu = 1.52 \times 10^{-6}\,\mathrm{m^2\,s^{-1}}$) drop of diameter $d_0 = 6\,\mathrm{mm}$ fall on the section of a solid iron cylinder with the same diameter. The drop is injected from an orifice that is 6 mm in diameter and is connected to an elevated plenum, and the falling height ranges from 5 to 130 cm. The experiment is conducted in a room safe from draughts to realize repeated centred impacts. A tube confining the drop trajectory is used for this purpose. The injection velocity is monitored to obtain 6 mm drops in all cases. The impacting velocity of the drop u_0 is set by varying both the injection velocity and the height of fall. The velocity ranges from 1 to $13\,\mathrm{m\,s^{-1}}$ (higher velocities cause the drop to deform in air and burst; see e.g. Villermaux & Bossa 2009 and the references therein) such that the Weber number

$$We = \frac{\rho\,u_0^2\,d_0}{\sigma} \qquad (2.1)$$

varies typically from 10^2 to 10^4, whereas the Reynolds number $u_0 d_0/\nu$ ranges from 10^3 to 10^5. The impactor is mounted on a translucent floor lit from below, and the

impact is recorded from the top at a weak parallax angle by a Phantom V5 camera operating at 1000 images s^{-1} and a resolution of 1024×1024 pixels.

Upon impact, the drop flattens into a radially expanding sheet which impales on the impactor while remaining attached to it in $r = r_0$, as seen in figures 2 and 3 . The impacted cylinder is fitted with a thin brass jacket to control the sheet ejection angle with respect to the solid cylinder axis (see Clanet & Villermaux 2002 for details) and is kept at right angle in the present study. The present set-up is the discrete version of the one initially studied by Savart (1833) with a continuous liquid jet and used in the context of drop impacts by Rozhkov *et al.* (2002, 2003, 2004). That configuration, where the sheet expands freely in a light environment at rest (namely ambient air), was chosen deliberately in order to avoid any interaction with solid wall, such as the formation of a viscous boundary layer. It does not remove the possible interaction with the surrounding gaseous environment, notably important when the drop expands over a solid surface (Xu *et al.* 2007) which is, we believe, unessential in the present case for reasons discussed below.

The chronology of the drop fragments' transformation, illustrated in figure 2, is as follows: the drop crushes on the impactor and feeds a radially developing sheet of radius $R(t)$, first expanding and then recoiling. The crushing time d_0/u_0 (2×10^{-3} s typically) is smaller than the typical time τ over which $R(t)$ varies (2×10^{-2} s typically) so that the details of drop deformation when it hits the solid are essentially decoupled from the subsequent dynamics of the sheet itself, when all the liquid initially contained in the drop is constitutive of the sheet. The average sheet radius increases up to a maximal value R_{max} which depends on u_0, while the sheet rim corrugates. These corrugations are the base for radial ligaments which, at the moment the sheet has been pierced by the impactor (second to last frame in figure 2) from which a hole opens and reaches the corrugated rim, collect most of the initial liquid drop and break to form stable drops. The overall transformation from the initial drop to stable fragments is completed shortly after the sheet rim has started to recede (i.e. when $\dot{R}(t) < 0$). The drop sizes were measured using the algorithm described in Marmottant & Villermaux (2004), and their distribution for the given conditions resulted from the accumulation of typically 10 impacts, representing typically 1000 resolved drops.

3. Expansion dynamics

Willing to achieve a transparent conclusion through a tractable analysis, we must deal with two *a priori* antagonist aspects of the phenomenon:

(i) It is clear that a spherical drop deposited on a surface at zero velocity keeps its shape and that its initial radius r_0 is not affected (provided it is small enough to disregard gravity). Hence, the effect of an impact at velocity u_0 results for $R(t) - r_0$ in a correction $F(u_0, t, \sigma, \ldots)$ which must vanish for $u_0 \to 0$. In other words, the expanded drop radius $R(t)$ *must* in the end be written as follows:

$$R(t) = r_0 + F(u_0, t, \sigma, \ldots). \tag{3.1}$$

(ii) The interesting case is obviously not the limit $u_0 \to 0$ but rather when the effect of the impact results in a strong shape change with a maximal radius extension $R_{max} \gg r_0$. In that case, the liquid constitutive of the drop shapes into a radially expanding sheet, whose typical thickness h is such that the aspect ratio h/R is very small, thus legitimating a slender-slope description. This limit is, in addition, what makes the problem easily tractable, but the final result should be compatible with (3.1).
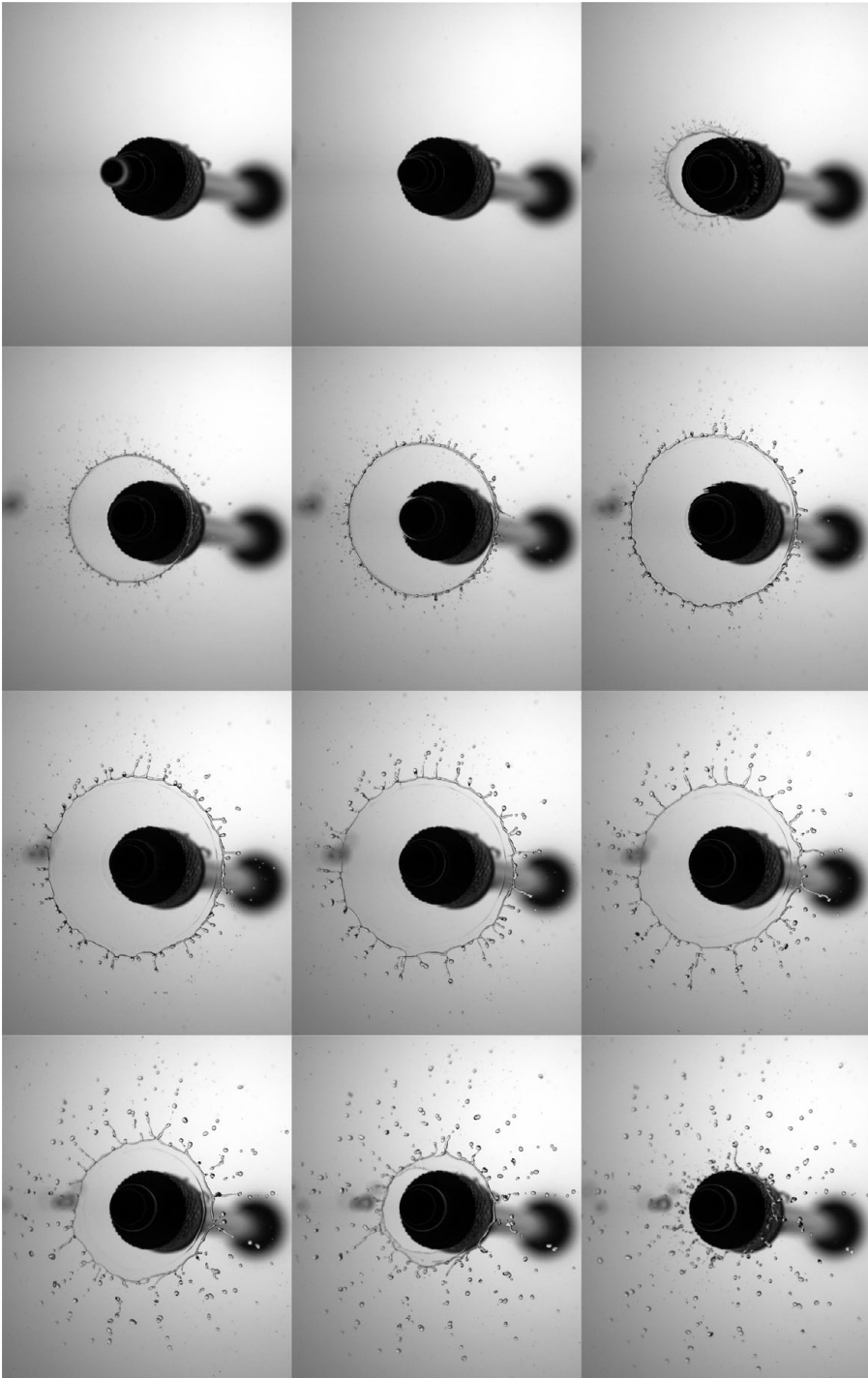
FIGURE 2. Sequence of events of the drop fragments' transformation following the drop (visible in the first image) impact on a target of the same diameter $d_0 = 6$ mm. The liquid is ethanol, and the Weber number is $We = 1200$. The time interval between the pictures is $1/500$ s.
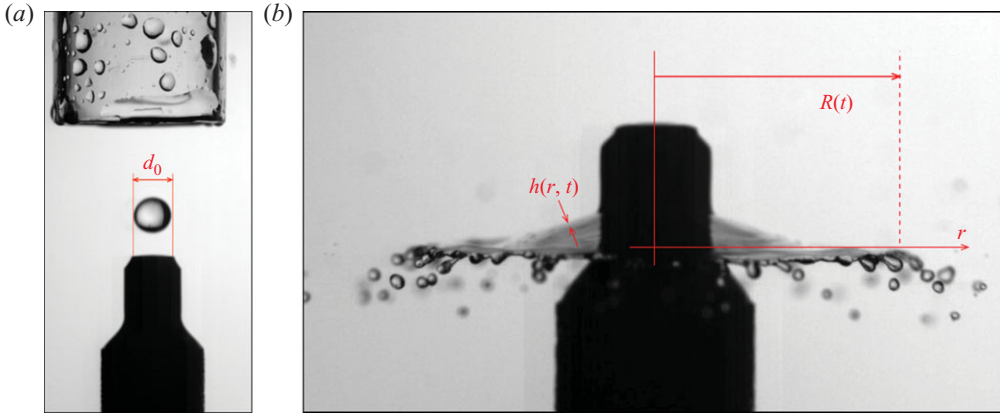
FIGURE 3. (Colour online) (*a*) A water drop just before it impacts the target of the same diameter $2r_0 = d_0 = 6\,\text{mm}$. Also visible is the confining tube used to prevent residual draughts from altering the drop trajectory. (*b*) Side view of the expanding sheet impaling on the impactor, $25/3000$ s after the impact of the drop for $We = 1800$, and definitions of the sheet thickness $h(r,t)$ and radius $R(t)$. The velocity $u(r,t)$ is the radial velocity in the sheet plane.

We call $u(r,t)$ and $h(r,t)$ the radial velocity and thickness of the expanding drop (figure 3), for which we write the Euler equation in the slender-slope approximation ($|\partial_r h(r,t)| \ll 1$):

$$\rho(\partial_t u + u\partial_r u) = -\partial_r p, \tag{3.2}$$

$$r\partial_t h + \partial_r(ruh) = 0, \tag{3.3}$$

where $p(r,t)$ is the pressure in the liquid. We do not consider any interaction with the surrounding gaseous environment in which it expands (see §4.4). An additional Trouton viscosity term (Trouton 1906; Taylor 1961)

$$6\eta\, \partial_r(hr\, \partial_r u)/(hr), \tag{3.4}$$

suitable for a biaxially stretched sheet, can be added to the right-hand side of (3.2) to account for viscous stresses in the liquid, which we neglect owing to the high value of the Reynolds number in the present case. A steady-state axisymmetric solution of (3.2) and (3.3) relevant to a continuous jet impacting a solid target is $u(r) = u_0$ and $h(r) = d_0^2/8r$, expressing global mass conservation and the conservation of energy carried by fluid particles from the jet to any radial location in the sheet (Clanet & Villermaux 2002). An impacting drop will produce a similar expanding sheet but with an *a priori* unknown injection rate; by extension, we thus seek for a time-dependent solution of the form

$$h(r,t) = \frac{f(t)}{r} \tag{3.5}$$

which, owing to (3.3) with the sheet remaining attached to the impactor as it expands and impales on it, that is $u(r_0,t) = 0$, implies

$$u(r,t) = -\frac{\dot{f}}{f}\,(r - r_0), \tag{3.6}$$

where $\dot{f}$ denotes $\mathrm{d}f(t)/\mathrm{d}t$. The fact that the (Eulerian) radial velocity in the sheet is an increasing function of r is consistent with figure 4 which shows how two initially close particles separate in time while keeping their initial (Lagrangian) radial
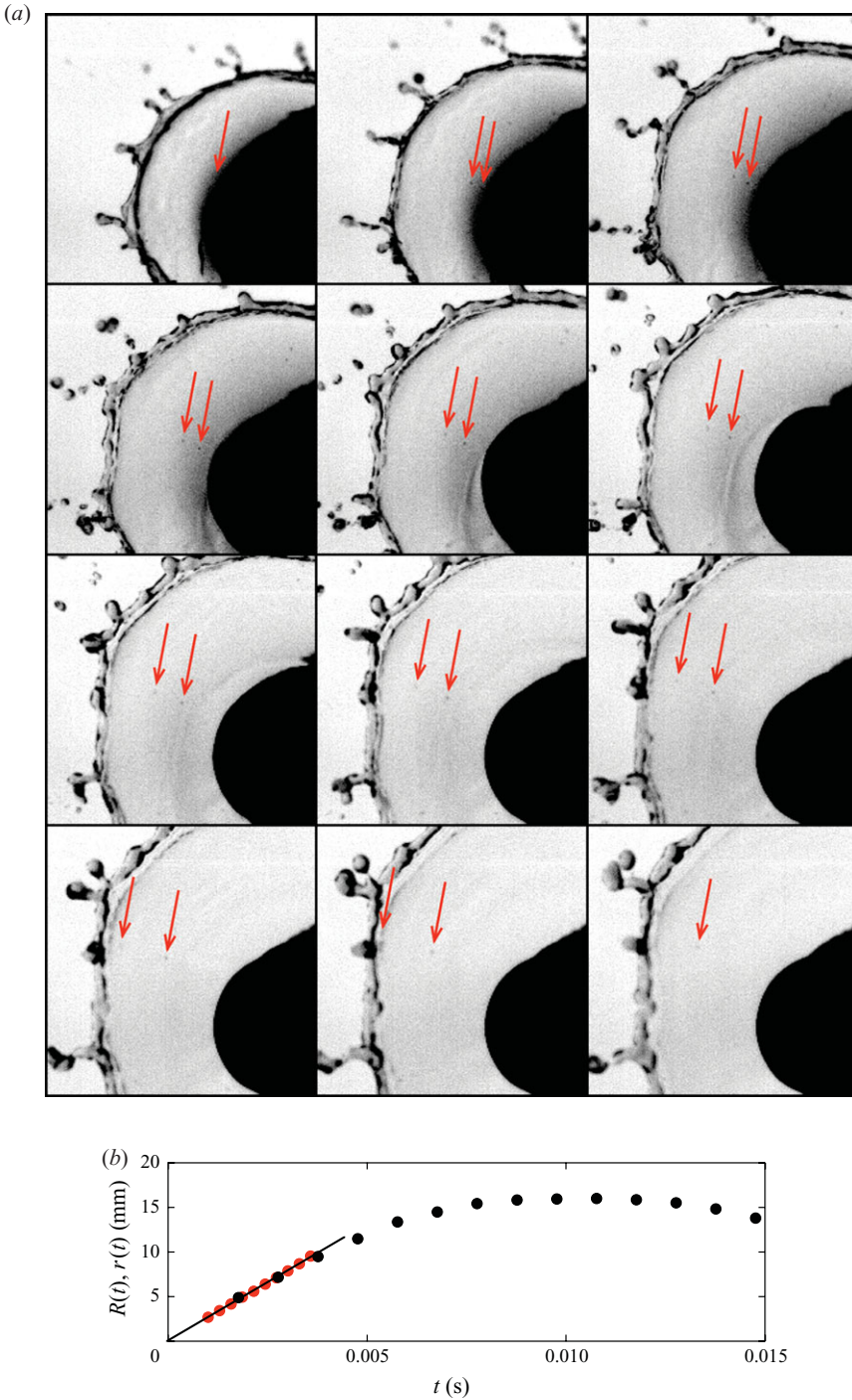
(a)

(b)

FIGURE 4. (Colour online) (a) Evidence for the radial dependence of the velocity $u(r,t)$: two initially nearby particles (smoke dust introduced in the liquid prior to drop formation) in the sheet separate along r as time elapses; $We = 800$, and time interval between the pictures is $2/3500$ s. (b) Time evolutions of the sheet radius $R(t)$ (black dots) and of the position $r(t)$ of a tracer particle in the sheet close to its edge and before it is incorporated in the rim (red dots), recorded simultaneously at $We = 10^3$. The black line represents $r(t) = u_0 t$.
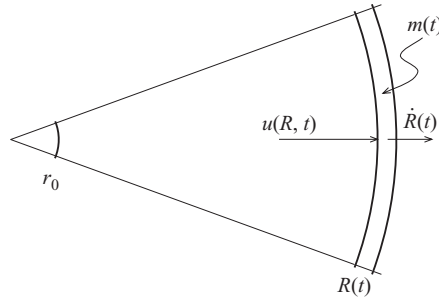
FIGURE 5. Sketch of the rim with mass per unit arclength, $m(t)$, attached to the sheet with velocity $u(r, t)$ and radius $R(t)$, used for the mass and momentum balances.

velocity as the sheet expands, an observation also made by Rozhkov *et al.* (2004) (see the discussion above (3.15)). The net radial flow rate transported along the sheet, $Q(r, t) = 2\pi r h(r, t) u(r, t) \sim r \dot{f}$, is thus expected to increase with r and to depend on time, by contrast with other choices made by Yarin & Weiss (1995) and Rozhkov *et al.* (2004); the latter authors postulated $Q(r) \sim 1/r$, independent of time, leading (see the discussion below (3.19); see also Appendix A) to very different trends for $h(r, t)$. Note that the viscous term in (3.4) identically cancels with the forms we have chosen for $h(r, t)$ and $u(r, t)$.

The solution for $f(t)$ is constrained by two additional conditions which express that the radially expanding fluid particles are arrested at some distance from the impact point $R(t)$ by capillary confinement and that they feed the sheet rim at which they progressively all collect (see e.g. figure 4). If $\Omega = \pi d_0^3/6$ is the initial drop volume, the liquid volume constitutive of the sheet at time t is

$$\int_{r_0}^{R} 2\pi r h(r, t) \, \mathrm{d}r = \Omega - \int_0^t 2\pi R(t)(u(R, t) - \dot{R}) h(R, t) \, \mathrm{d}t, \tag{3.7}$$

where the second term on the right-hand side of is the net volume accumulated at time t on the rim. Momentum conservation at the rim whose mass per unit arclength is $m(t)$ is written (see figure 5) according to a system familiar in the propulsion context (Tsiolkovsky 1903):

$$\frac{\mathrm{d}}{\mathrm{d}t}(mR \cdot \dot{R}) = qu(R, t) R - 2\sigma(R - r_0), \tag{3.8}$$

$$q = \rho h(R)(u(R, t) - \dot{R}) \tag{3.9}$$

with

$$q = \frac{1}{R} \frac{\mathrm{d}}{\mathrm{d}t}(mR) \tag{3.10}$$

in axisymmetric coordinates. Equation (3.8) expresses that the rate of change of the rim inertia is equal to the sum of the momentum it absorbs plus the net force acting on it. The velocity $u(R, t)$ is that of the liquid in the sheet at $r = R(t)$ in the Galilean reference frame of the laboratory. The force term $2\sigma(R - r_0)$ incorporates the initial drop radius r_0 and vanishes when $R = r_0$; indeed, the net force acting on an immobile drop of radius r_0 is zero, in compliance with constraint (3.1). Equations (3.9) and (3.10) express the conservation of mass. It will be shown below (see §4.2) that $m\ddot{R}$

can be neglected because $|(m\dot{R})/mR| \gg |\ddot{R}/\dot{R}|$ for all times. Thus, (3.8) amounts to

$$\rho h(R)(u(R,t) - \dot{R})^2 = 2\sigma\left(1 - \frac{r_0}{R}\right),\tag{3.11}$$

reminiscent of Culick's law (Culick 1960). Using (3.5) and (3.6) for $h(r,t)$ and $u(r,t)$, one gets from (3.7) and (3.11)

$$f(t)[R(t) - r_0] = \frac{\Omega}{2\pi}\left(1 - \frac{t}{\tau}\right)^2\tag{3.12}$$

with

$$\tau = \sqrt{\frac{\rho\,\Omega}{\pi\sigma}}.\tag{3.13}$$

Integrating the momentum equation (3.2) between $r = r_0$ and $r = R(t)$ with (3.6) for $u(r,t)$ yields

$$\frac{(R(t) - r_0)^2}{2}\left(-\frac{\ddot{f}}{f} + 2\left(\frac{\dot{f}}{f}\right)^2\right) = -\frac{1}{\rho}\left\{p(R,t) - p(r_0,t)\right\}.\tag{3.14}$$

The pressure in the liquid is the ambient pressure p_{atm}, taken as independent of r, since we disregard any interaction with the ambient medium as well as viscous stresses, plus a correction, owing to Laplace law, accounting for the liquid interface curvature. That curvature is weak and decays in time for most of radial location $r < R(t)$, where it is of the order of $\partial^2 h/\partial r^2 \approx \Omega/R^4$. The liquid interface curvature is comparatively larger at the sheet rim, but there, recirculation motions dissipate energy in a way that the internal pressure is not likely to increase compared with its value in the quasi-planar sheet attached to it, as discussed in Appendix B. The pressure in the liquid is thus essentially constant along r, that is $p(R,t) \approx p(r_0,t)$.

The absence of pressure gradient along r induces a ballistic motion of the fluid particles. Equation (3.14) with the right-hand side set to zero is indeed a reformulation of $u(r, t + \delta t) = u(r - \delta r, t)$, expressing velocity conservation, or equivalently of (3.2) for $\partial_r p = 0$, with $\delta r/\delta t = u(r,t)$ given by (3.6). It is consistent with the observed fact that tracer particles indeed keep their initial velocity while travelling along the sheet (figure 4). Under this assumption, which cancels the right-hand side of (3.14), and using (3.13), one gets

$$\ddot{R} + \frac{6}{(\tau - t)^2}(R - r_0) + \frac{4}{\tau - t}\dot{R} = 0.\tag{3.15}$$

Equation (3.15) interestingly shows that the nonlinear dynamics of (3.2) and (3.3) leads to a linearly damped oscillatory motion of the sheet radius, with time-dependent frequency and damping factor. This dynamics expresses a simple balance between inertia (that of the initial drop) and capillary restoring forces (through Culick's law), the damping term originating from the continuous transfer of momentum from the sheet to the rim.

For times of the order of $d_0/u_0 \ll \tau$, the radial velocity of the fluid particles at the impactor edge in $r_0 = d_0/2$ is u_0, as seen in figure 4 and as expected from energy conservation along the curved streamline going from the heart of the crushing drop to the expanding sheet (this result also holds for the continuous Savart case; see Clanet
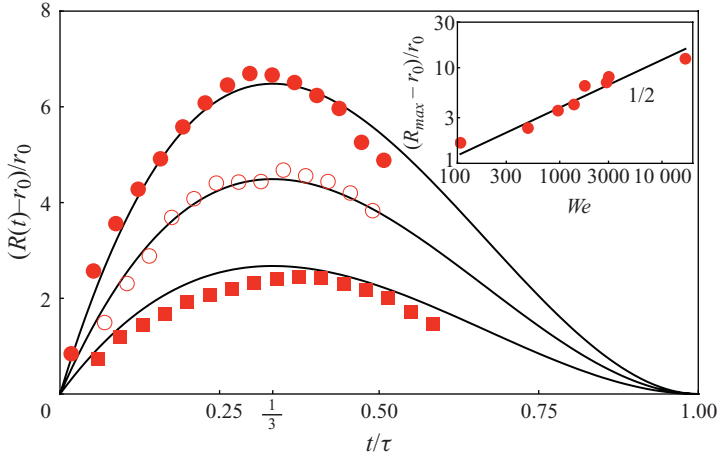
FIGURE 6. (Colour online) Sheet radius evolution as a function of dimensionless time t/τ for three different impact Weber numbers, $We = 489$ (■), 1378 (○) and 2873 (●), superimposed with the trajectory expected from (3.16). The insert shows the dependence of the maximal sheet extension R_{max} on the Weber number. The line represents (3.18).

& Villermaux 2002). Thus with $R(0) = r_0$ and $\dot{R}(0) = u_0$, the radius of the expanding drop is expected to be

$$\frac{R(t) - r_0}{r_0} = \sqrt{\frac{2}{3}} \sqrt{We} \, \frac{t}{\tau} \left(1 - \frac{t}{\tau}\right)^2, \tag{3.16}$$

describing an asymmetric one-period oscillatory motion which fits well the observed trajectories for different Weber numbers (figure 6) and which lasts for

$$\tau = \sqrt{\frac{\rho \, d_0^3}{6 \sigma}}. \tag{3.17}$$

This period is proportional to the Rayleigh time characteristic of drops oscillating slightly around their spherical stable shape, a time scale holding also, at least in scaling dependencies, for even larger deformations, as noticed earlier about drops impacting a hydrophobic surface (Richard, Clanet & Quéré 2002) or a solid above the Leidenfrost temperature (Watchers & Westerling 1966). The trajectory $R(t)$ is usually found to be much more asymmetric when the drop impacts a solid surface (Chandra & Avedisian 1991; Bartolo, Josserand & Bonn 2005) because the viscous stress at the wall slows down the recoil period.

The maximal amplitude of the motion is reached for $t/\tau = 1/3$ and is

$$\frac{R_{max} - r_0}{r_0} = \frac{4}{27} \sqrt{\frac{2}{3}} \sqrt{We} \approx 0.12 \sqrt{We}, \tag{3.18}$$

a law fitting the observed maximal radii not only in scaling dependencies (see also Chandra & Avedisian 1991; Roisman, Riobo & Tropea 2002; Rozhkov *et al.* 2002, 2004; Mehdizadeh, Chandra & Mostaghimi 2004; Ukiwe & Kwok 2005) but also quantitatively, including the prefactor (the insert of figure 6). Note that $R_{max} = r_0$ for $We \to 0$, as it should for a small drop (not deformed by gravity) deposited gently on a solid surface (consistently, $\ddot{R} = 0$ for $R = r_0$ and $\dot{R} = 0$ in (3.15)).

The trajectory $R(t)$ in (3.16) together with (3.13) thus provides a representation for the motion within the sheet $u(r, t)$ and for its thickness $h(r, t)$ as

$$u(r, t) = \frac{r}{t}, \quad h(r, t) \sim \frac{\Omega}{u_0 \, rt}, \tag{3.19}$$

giving a carried flow rate $Q(r, t) = 2\pi rh(r, t) \sim \Omega r/(u_0 t^2)$. The flow description in (3.19) is at odds with the one in Rozhkov *et al.* (2004) who, postulating $Q(r) \sim 1/r$ and ballistic motion along r, obtained $u(r, t) \sim r/t$ and $h(r, t) \sim t/r^3$. That description which, unlike the present one, also incorporates several adjustable parameters offers a much poorer agreement, as it overestimates the radius trajectory $R(t)$ at late times, a consequence of the presumed *increase* in sheet thickness in time. The flow in (3.19) is also different from the one in Yarin & Weiss (1995) who, from a different approach (see also Appendix A), arrive at $u(r, t) \sim r/t$ and $h(t) \sim 1/t^2$.

A few final remarks are in order:

(i) The consistency of the present model for $R(t)$ is ensured by the large value of the Weber number $\sqrt{We} \sim \tau/(d_0/u_0)$ expressing the time scale separation between the liquid reorganization at the impact that we do not describe (lasting d_0/u_0) and the comparatively long inertia–capillary expansion and recoil dynamics of the deformed drop (lasting τ).

(ii) The present solution is highly dissipative. Indeed, from a naive global energy conservation $(1/2\rho u_0^2 \pi d_0^3/6 \sim 2\sigma \pi R_{max}^2)$, it would be expected that $R_{max}/r_0 \sim \sqrt{We/6} \approx 0.4\sqrt{We}$, an extension much larger than the real one in (3.18). Dissipation does not occur at the impact location, nor in the sheet, whose motion is conservative, but at the rim where all the incoming kinetic energy of the particles absorbed in the rim is basically dissipated (see Appendix B).

(iii) Gravity, although responsible for accelerating the drop up to its impacting velocity u_0, is subdominant in the dynamics for $R(t)$. The typical acceleration (in the sheet plane) is of order u_0/τ, and denoting $Fr = u_0^2/(g \, d_0)$ the Froude number, one has

$$\frac{u_0}{g\tau} = \frac{Fr}{\sqrt{We}} = O(10^2). \tag{3.20}$$

The radius trajectories are interrupted at $t/\tau \approx 0.6$ because the rim has destabilized (figure 6). The parameters needed to understand this destabilization kinetics are those describing $R(t)$ according to (3.16), as shown below.

4. Stability and ligament formation

As the sheet expands, its border gets more corrugated (figure 7). We denote ξ the amplitude of the corrugation, which depends on time t and the azimuthal location along the rim θ. In a local frame tangent to the rim, we have in a planar approximation $\xi \sim e^{ikx - i\omega t}$ with $x = R\theta$, valid for $kR \gg 1$. Corrugations grow on their own, but the natural length scale to measure the growth of the amplitude ξ is the sheet radius R itself: the destabilization of the sheet has occurred when the corrugations of its edge represent a substantial fraction of its radius. With that reference scale, the growth of the amplitude is written as (see also Tomotika 1936 in the context of stretching jets)

$$\frac{d}{dt} \ln\left(\frac{\xi}{R}\right) = -\frac{\dot{R}}{R} + \text{Re}(-i\omega), \tag{4.1}$$
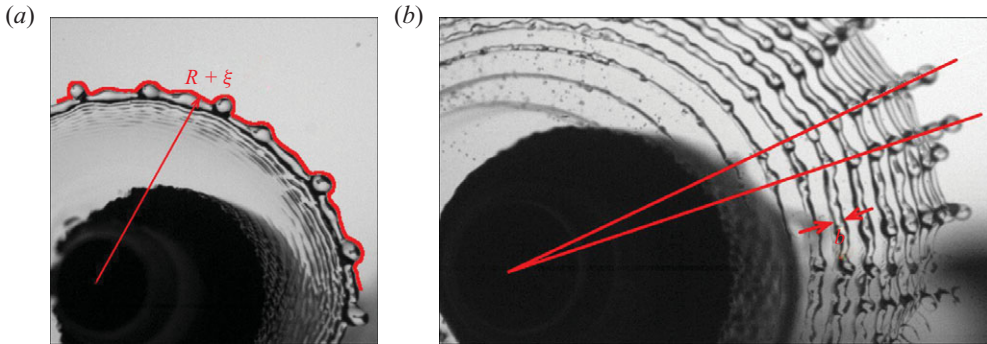
FIGURE 7. (Colour online) (*a*) Rim destabilization and the amplitude of corrugation, ξ. (*b*) Superimposed pictures of the sheet taken at constant time interval, showing sheet radius slowing, rim destabilization, rim diameter *b* constancy and wavenumber stretching.

where $\mathrm{Re}(-i\omega)$ is the growth rate of the instability responsible for the rim corrugations; it has to be large enough to overcome the geometrical damping $-\dot{R}/R$, for ξ to increase.

4.1. *A global Rayleigh–Taylor mechanism is unlikely*

The particles close to the sheet rim are part of an ever-decelerating density interface. This situation, as noted by Simpkins & Bales (1972), Allen (1975), Kim, Feng & Chun (2000) and others, may be unstable in the sense of Rayleigh–Taylor, since the associated body force, if present, would be pointing towards the light medium (namely the surrounding gas).

However, there is, according to the solution for $R(t)$ derived above, no pressure gradient along r at all and hence no net body force. Indeed

$$\partial_r p = -\rho \left(-\frac{\ddot{f}}{f} + 2 \left(\frac{\dot{f}}{f} \right)^2 \right) r \tag{4.2}$$

$$= 0, \tag{4.3}$$

since (3.14) with $p(R,t) = p(0,t)$ cancels the right-hand side of (4.2). The expansion and recoil dynamics is essentially made at constant pressure, the inertia of the liquid being balanced by a restoring force concentrated at the rim edge, according to Culick's law. Further arguments discussed in Appendix B suggest that the dissipation in the rim, although the fluid is arrested there, prevents its internal pressure to increase appreciably (in a Galilean frame; see however §4.3). Thus, although its rim is decelerating for most of its development period ($\ddot{R}(t) < 0$), a *global* Rayleigh–Taylor instability of the expanding sheet is unlikely, because most of the liquid in the sheet does not feel this deceleration which only affects the fluid particles in the rim and where the instability takes place, as explained in §4.3.

4.2. *Fast capillary destabilization of the rim*

The rim becomes rapidly thick compared with the sheet to which it is attached. It is gradually fed by more incoming liquid from the sheet (the difference $u(R,t) - \dot{R}(t)$ is always positive; see e.g. figure 4); it is also stretched, since it borders a frontier expanding like $R(t)$. By the combination of these two effects, its diameter b (figure 7) reaches an equilibrium value. The volume accumulated in the rim is such that
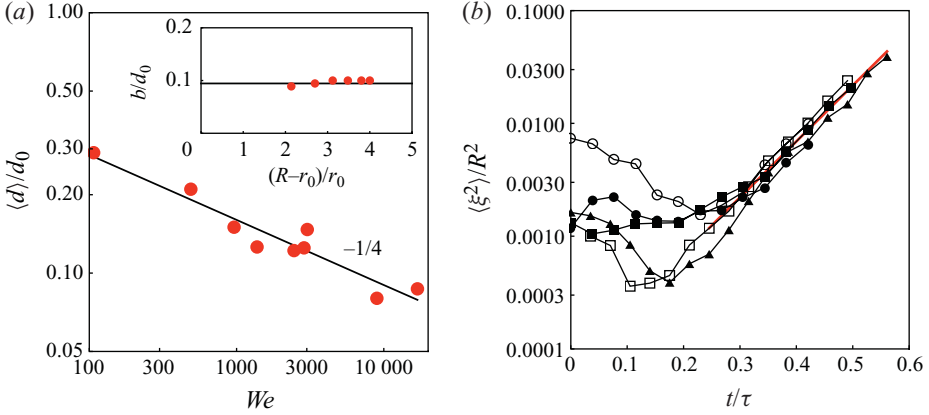
FIGURE 8. (Colour online) (*a*) Average fragment drops' diameter $\langle d \rangle$ as a function of the impacting Weber number; $d_0 = 6\,\text{mm}$. The insert shows the rim diameter b scaled by the initial drop diameter d_0 as a function of current radius $R(t)$ for $We = 1200$. (*b*) Time evolution of the rim corrugations scaled by the sheet radius $\langle \xi^2 \rangle / R^2$ for different impact Weber numbers, $We = 490\,(\bullet)$, $960\,(\circ)$, $1400\,(\blacksquare)$, $2460\,(\square, \blacktriangle)$. The red line indicates exponential growth.

(see (3.7))

$$\frac{\pi^2}{2} b^2 R = \Omega - \int_{r_0}^{R} 2\pi r h(r, t)\, \mathrm{d}r, \tag{4.4}$$

providing

$$\frac{\pi^2}{2} b^2 R = \Omega (1 - (1 - t/\tau)^2) \approx 2\Omega t/\tau. \tag{4.5}$$

With $R \sim \sqrt{We}\, t/\tau (1 - t/\tau)^2 \approx \sqrt{We}\, t/\tau$ on the same time interval in the growth period, one anticipates that

$$b \sim d_0\, We^{-1/4} \tag{4.6}$$

independent of time, as seen in figure 8. The rim is likely to destabilize by fluid rearrangements driven by capillarity, in a way similar to a Plateau–Rayleigh mechanism (see e.g. Bremond & Villermaux 2006). The associated time scale of this capillary instability is

$$\tau_c \sim \sqrt{\frac{\rho\, b^3}{\sigma}} \sim \tau\, We^{-3/8} \ll \tau, \tag{4.7}$$

much smaller than the overall sheet–drop transition period τ and soon also smaller than the stretching time $R/\dot{R} \sim t$ which therefore does not affect its development as soon as $t/\tau > We^{-3/8}$. Note that the rim mass per unit arclength, $m \sim \rho b^2$, is constant, thus supporting the assumption leading to (3.11).

4.3. *Radial expulsion from the rim*

The fast destabilization of the rim accounts for the corrugations soon visible at the sheet edge. However, the sheet ultimately fragments via the formation of ligaments which are ejected radially in the plane of the sheet, in a way very similar to the Edgerton crown phenomenology. The origin of this 'radial expulsion' has yet to be understood.

The pressure is constant along the sheet up to $r = R(t)$ even with $\ddot{R} \neq 0$. It would remain essentially constant *in the rim* too if the acceleration $\ddot{R}$ were zero (see

Appendix B). But since the rim sits in a decelerating frame, an associated body force proportional to $-\rho\ddot{R}$ exists, which pushes the fluid particles constitutive of the rim radially outward. This force, which originates in the non-Galilean character of the rim motion, induces a Rayleigh–Taylor-like mechanism, but localized at the rim.

With an acceleration in the plane of the sheet $-\ddot{R}$, the growth rate of perturbations of the rim location with wavenumber k reads, in the planar approximation and in the infinite depth limit (i.e. when $kR \gg 1$; see Bremond & Villermaux 2005),

$$\omega^2 = \ddot{R}k + \frac{\sigma}{\rho}k^3 \qquad (4.8)$$

with $\ddot{R} < 0$, which also reads

$$\omega^2 = -\frac{\ddot{R}}{a}(-ka + (ka)^3) \qquad (4.9)$$

with $a = \sqrt{\sigma/\rho(-\ddot{R})}$. The perturbations are themselves carried by fluid particles which separate geometrically during the sheet expansion (see figure 7 and Thoroddsen & Sakakibara 1998) so that a wavenumber k_0 on the rim at, say, $R = r_0$ will be stretched by the base flow according to

$$kR = k_0 r_0. \qquad (4.10)$$

The instantaneous growth rate of an initial perturbation of wavenumber k_0 is thus

$$\omega^2 = -\frac{\ddot{R}}{R}k_0 r_0\left(-1 + (k_0 r_0)^2 \frac{a}{R}\right). \qquad (4.11)$$

The net gain of a perturbation with initial wavenumber k_0 results from the integration of the above instantaneous growth rate with the known temporal dependencies of $R(t)$ and $\ddot{R}(t)$ (see e.g. Eggers & Villermaux 2008). It is however clear that a perturbation amplitude $\xi(k_0, t)$ with $k_0 r_0 = \mathcal{O}(1)$ has a growth rate proportional to $\text{Re}(-i\omega) \approx \sqrt{-\ddot{R}/R}$ and that, according to (4.1), it will grow like

$$\frac{\mathrm{d}}{\mathrm{d}t}\ln\left(\frac{\xi}{R}\right) = -\frac{\dot{R}}{R} + \sqrt{\frac{-\ddot{R}}{R}}. \qquad (4.12)$$

Figure 8 shows the time dependence of the mean squared amplitude $\langle\xi^2\rangle$. The local radius is $R + \xi$, as shown in figure 7, and the brackets stand for an average over the radial positions θ at a given instant of time. Obviously, $\langle\xi\rangle = 0$. The perturbation amplitude relative to R first decays because of the intense stretching at short time ($\dot{R}/R \sim 1/t$) and then grows. The stretching vanishes close to the maximal sheet extension when $\dot{R} = 0$. At that time ($t/\tau = 1/3$), the deceleration of the rim $\ddot{R}$ is such that

$$\frac{\ddot{R}}{R} = -\frac{27}{2}\frac{1}{\tau^2}, \qquad (4.13)$$

leading to a growth of the radial ligaments amplitude *independent* of the impacting velocity. The growth of the rim indentations is thus ruled by the same time scale τ as the one ruling the sheet expansion itself, explaining why the sheet rim breaks in a time (of the order of $t/\tau \approx 0.6$), independent of the Weber number. The optimal wavenumber making ω^2 extremum is

$$k_c \sim \frac{1}{a} = \sqrt{\frac{R}{\Omega}}, \qquad (4.14)$$

providing

$$k_c d_0 \sim We^{1/4}, \tag{4.15}$$

close to the maximal sheet extension in $R = R_{max} \sim d_0 We^{1/2}$ where the damping $-\dot{R}/R$ is zero. The corresponding wavelength coincides, at least in law, with the one arising from the capillary destabilization of the rim whose diameter b is given by (4.6). Interestingly, the unstable capillary corrugations of the rim are 'expulsed' at a wavelength matching their own wavelength, explaining why it is so difficult to decipher between the two kinds of instabilities in practice (see Bremond & Villermaux 2006; Roisman *et al.* 2006; see also the discussion in Krechetnikov 2010). Since they are expelled from the rim close to the maximal sheet extension, the number N of ejected ligaments is expected to scale as

$$N \sim k_c R_{max} \sim We^{3/4}, \tag{4.16}$$

a scaling consistent with our observations and with the one found for drops impacting a solid surface (Marmanis & Thoroddsen 1996). The measurements of Cossali, Coghe & Marengo (1997) exhibit, however, a weaker dependence on We. Not surprisingly, this characteristic size also sets the average drop size in the resulting spray,

$$\langle d \rangle \sim d_0 We^{-1/4}, \tag{4.17}$$

for those arising from the breakup of corrugated ligaments whose transverse size is b, as seen in figure 8.

4.4. *Interplay with ambient air*

A liquid sheet expanding in an environment (air in the present case) at rest is known to interact with it (Squire 1953). That interaction, of a Kelvin–Helmoltz type, confers to the sheet a flapping motion around a wavelength λ, equilibrating air inertia $\rho_a u_0^2$ if u_0 is the characteristic velocity difference between the in-plane motion of the sheet and its surroundings, and capillary restoration forces σ/λ. Here, the prefactors matter and we keep them (see Villermaux & Clanet 2002 for the mode selection in a radially expanding sheet with a thickness profile $h(r) \sim 1/r$):

$$\lambda = \frac{10\pi\sigma}{\rho_a u_0^2}. \tag{4.18}$$

This instability is likely to develop and therefore alter the sheet dynamics if at least one wavelength λ exists within, say, the radial interval between $r = 0$ and $r = R_{max} \approx 0.12 (d_0/2) We^{1/2}$. The condition $\lambda < R_{max}$ is fulfilled above a critical Weber number $We^\star$ such that

$$We^\star = \left(\frac{20\pi}{0.12} \frac{\rho}{\rho_a} \right)^{2/3} \approx 5 \times 10^3 \tag{4.19}$$

for a water droplet expanding in air at atmospheric pressure. This Weber number is close to the largest values investigated in this study so that the presence of an external medium is unlikely to influence the phenomena described here. The same conclusion holds when comparing the flapping instability time of development (see Villermaux & Clanet 2002) with τ. We have indeed seen no sign of flapping at all. This interaction with air may however be relevant at the very first moments of the contact of the drop with the solid when the first 'ejecta sheet' is both very thin and fast (Xu *et al.* 2007; Pepper, Courbin & Stone 2008). But this is confined to very short instants of time (smaller than d_0/u_0) and is not concerned with the dynamics described here.
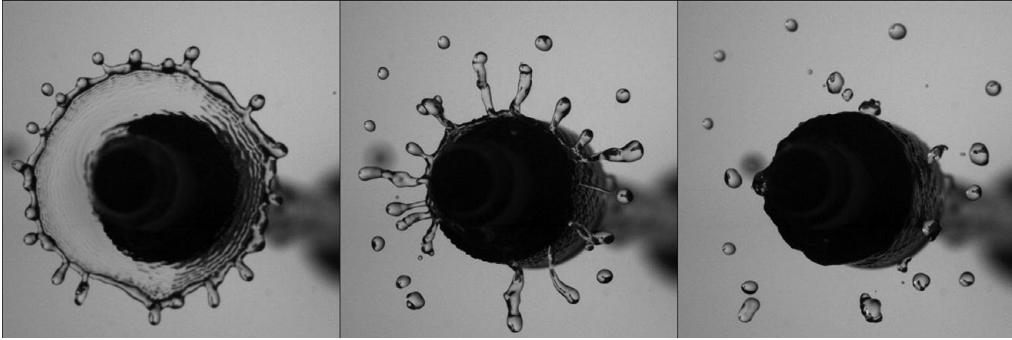
FIGURE 9. Construction of the elementary drop size distribution from the breakup of similar ligaments. The first image is a snapshot taken close to the maximal sheet extension $1/100$ s after drop impact. The time interval between the images is $1/100$ s; $We = 490$.

5. Drop size distributions

5.1. *Elementary distributions from ligament breakup*

Sprays are built from the breakup of ligaments. Depending on the way the ligaments have been prepared, precisely depending on their initial roughness, the distribution of sizes d in the spray is more or less broad. The distribution coming from ligament breakup is of a gamma type,

$$\Gamma(n, x = d/\langle d \rangle) = \frac{n^n}{\Gamma(n)} x^{n-1} e^{-nx}, \qquad (5.1)$$

with a parameter n being the function of the ligament corrugation. As explained in Villermaux (2007), this distribution does not result from the maximization of an entropy (which would give a distribution with a much too rapidly falling large excursion tail), nor does it reflect a sequential multiplicative process (which would give a log-normal distribution). It originates from the rearrangement dynamics of the fluid particles along the ligament as the ligament separates into disjointed drops. The index n refers to the roughness of the ligament: a straight, smooth ligament has $n = \infty$ and produces a single-size population of drops. A strong corrugation means that the amplitude of the cross-section diameter fluctuations along the ligament is of the order of its mean radius. In that case, the parameter n is of order of a few units, typically 4–5.

These corrugated ligaments are those produced by the radial expulsion from the sheet rim, as seen in figure 9. The corresponding distribution of sizes $P(d)$, obtained for a moderate impact Weber number $We = 490$ is indeed observed to be

$$P(d) = \frac{1}{\langle d \rangle} \Gamma(5, d/\langle d \rangle) \qquad (5.2)$$

with an order $n = 5$ (figure 10), identical to the one observed for a continuous jet impacting a solid target, expanding radially and then fragmenting into drops via corrugated ligaments (see figure 23 in Bremond, Clanet & Villermaux 2007). This is the 'elementary' distribution obtained when all the ligaments carry the same volume of fluid and have the same level of corrugation, that is when they all break with a mean drop size $\langle d \rangle$. This distribution is similar in shape with those commonly measured in drop impacts (Stow & Stainer 1977; Mundo *et al.* 1995; Yarin & Weiss 1995; Roisman *et al.* 2006) and is probably a good quantitative fit for them.
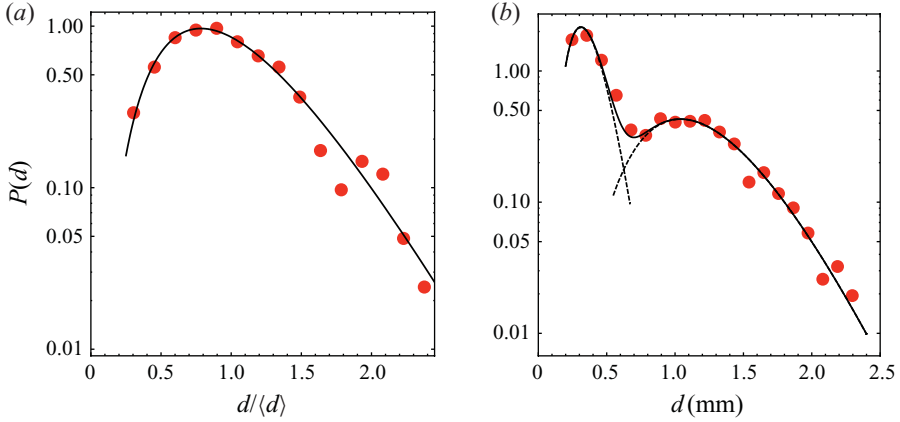
FIGURE 10. (Colour online) (*a*) Elementary distribution $P(d)$ obtained for $We = 490$ and fit according to (5.2). (*b*) Compound distribution obtained at $We = 1400$ under very symmetrical conditions (see figure 11) and fit according to (5.3).

5.2. *Composition law and global distributions*

The poly-dispersity of the drops in a given spray may result both from the distribution of the drops coming from the breakup of a given ligament and from the distribution of the volumes carried in the population of the ligaments. Several particular cases exhibit a homogeneous population of ligaments, all carrying the same volume so that the poly-dispersity of the drop sizes in the spray is contained by that arising from the breakup of a single ligament (see e.g. Marmottant & Villermaux 2004; Bremond & Villermaux 2006). There is, however, no reason that this should be a general rule.

The present experiment offers an example in which the overall spray is a mixture of the elementary distribution in (5.1) and of the distribution of ligament volumes or the equivalent mean diameter. For a very symmetrical impact at $We = 1400$, the sheet expands radially, thins and eventually impales on the solid impactor. A hole expands from the impactor to the rim, which at the same time forms radial ligaments. Two distinct classes of ligaments are formed, one with mean $a_1 = 0.35$ mm coming from the remnant rim not completely converted into radial ligaments, and the other with mean $a_2 = 1.17$ mm corresponding to the thick radial ligaments (figure 11). They both break to form a dispersion of drops around their respective averages (figure 10). The ligaments with the smallest mean a_1 are more numerous than those with the largest mean a_2 in a ratio close to 3/2. The linear superposition of the two elementary gamma distributions centred around their respective means leads to a *compound* overall distribution as

$$P(d) = \frac{0.6}{a_1}\, \Gamma(9, d/a_1) + \frac{0.4}{a_2}\, \Gamma(9, d/a_2). \tag{5.3}$$

This sheet piercing is quite a deterministic event and forms the two classes of ligaments evidenced in figure 11 when the impact is absolutely perfectly centred. Any tiny off-centre deviation produces a continuous distribution of ligament sizes. If now the ligaments' equivalent average size a is distributed according to $q(a/\langle d \rangle)$, where $\langle d \rangle$ is the average size of the ligament population, the drop size distribution in the spray
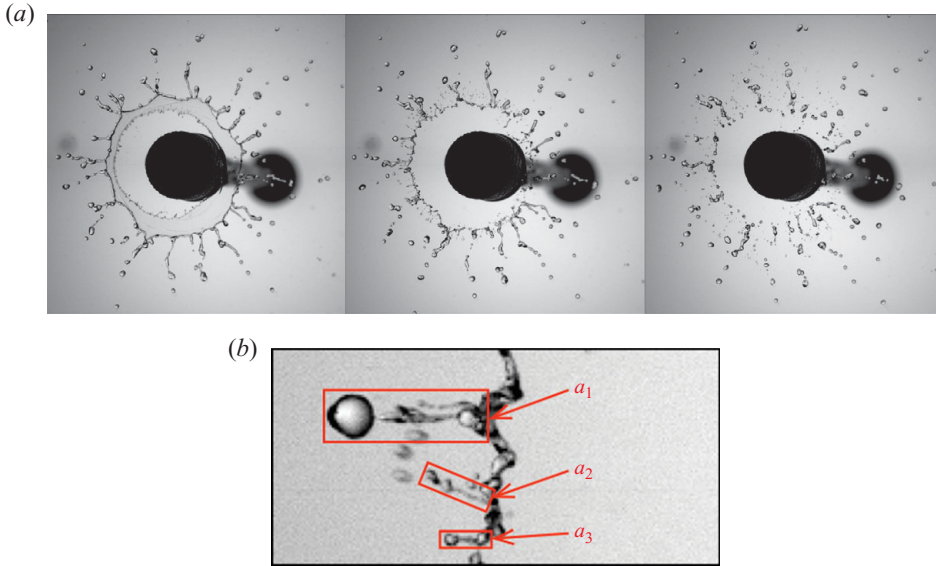
(*a*)

(*b*)

FIGURE 11. (Colour online) (*a*) Compound fragmentation under very symmetrical impact at $We = 1400$. The time interval between the images is $1/1000$ s. Two distinct classes of ligaments are formed, one with mean $a_1 = 0.35$ mm coming from the remnant rim not completely converted into radial ligaments, and the other with mean $a_2 = 1.17$ mm corresponding to the thick radial ligaments (see also figure 10). (*b*) A family of homothetic (i.e. having the same aspect ratio) ligaments with a continuous distribution of equivalent sizes a_i with $i = 1, 3$.

will be

$$P(d) = \int q(a/\langle d \rangle) \, p(d/a) \, \mathrm{d}a. \tag{5.4}$$

How is a generically distributed? Remembering that, in the present case, ligaments are expelled from the sheet rim and that the rim is itself a toroidal ligament, it is clear, except for special conditions like the ones described above, that the distribution of the ligament sizes will follow the distribution of the corrugations of the rim, itself characteristic of a ligament, and that a will be continuously gamma-distributed (figure 11) as

$$q(a/\langle d \rangle) = \frac{1}{\langle d \rangle} \, \Gamma(m, a/\langle d \rangle), \tag{5.5}$$

where $\langle d \rangle$ is the average ligament size given in (4.17). With drop sizes distributed according to (see (5.1))

$$p(d/a) = \frac{1}{a} \, \Gamma(n, d/a) \tag{5.6}$$

for a ligament of size a, we have, following the linear superposition of (5.4),

$$P(x = d/\langle d \rangle) = \frac{2m^m n^{(m+n)/2} (mx)^{(n-m)/2} x^{m-1} \mathrm{K}_{m-n}(2\sqrt{nmx})}{\Gamma(m)\Gamma(n)}, \tag{5.7}$$

where K_{m-n} is the Bessel function of order $m - n$ (Abramowitz & Stegun 1964). This global fragment size distribution incorporates two *a priori* free parameters, namely m, setting the width of the rim corrugations' distribution, and n, setting the distribution of the ligament corrugations. These parameters are, in practice, constrained. As already mentioned, the ligaments forming drops are strongly corrugated so that $n \approx 5$. The
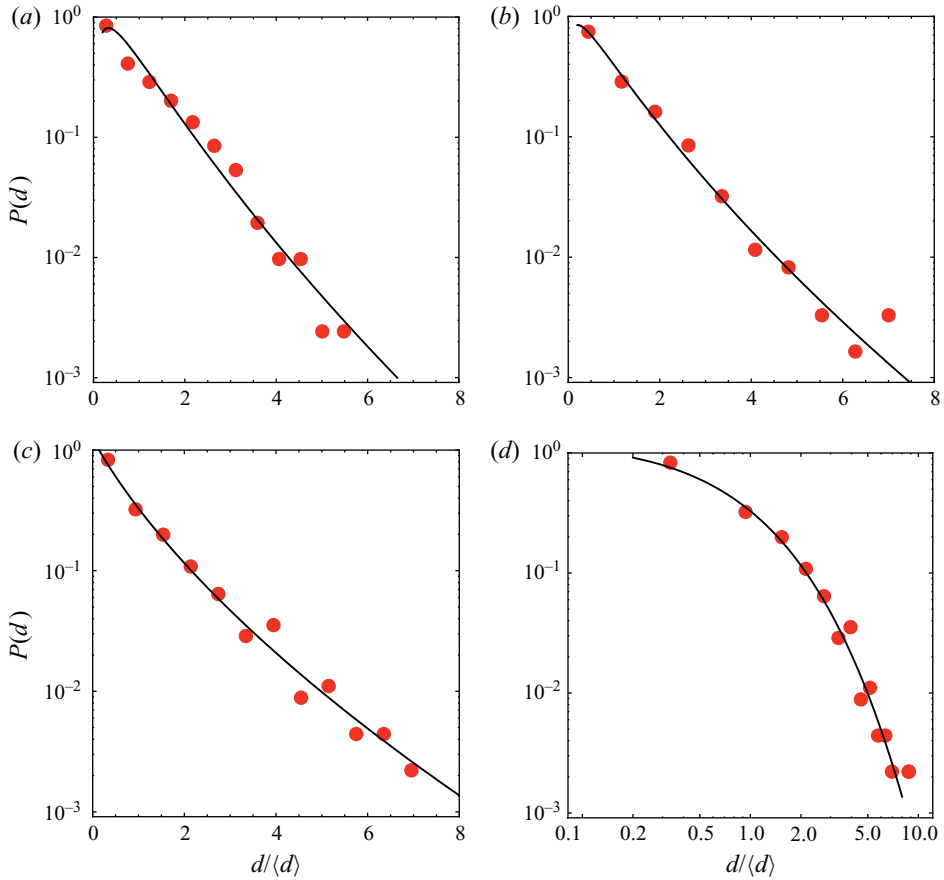
FIGURE 12. (Colour online) Global drop size distributions $P(d)$ obtained for increasing Weber numbers, $We = (a)$ 960, (b) 2870 and (c) 16 930. Also shown is the distribution at (d) $We = 16\,930$ in log–log units. The solid line is a fit by (5.7) with $n = 5$ and $m = 2$, 1.5 and 1 ($We = 960, 2870$ and $16\,930$ respectively).

same limit applies generically to the rim corrugations, and we find indeed that, taking n equal to 5, the values of m fitting the experimental distributions are of the order of 1–2 for Weber numbers in the range 960–16 930 (figure 12).

The overall drop size distribution is thus a compound of stable drops coming from the breakup of ligaments essentially exponentially distributed in size, a phenomenon also encountered for the 'soft' impact of drops bursting because of a relative motion in air (Villermaux & Bossa 2009). Note that, in this limit, the drop size distribution $P(d)$ is broader than an exponential law but narrower than a pure power law, as seen in figure 12.

6. Conclusion

We have described the complete sequence of events accompanying the transition from an initially compact drop impacting a solid target matching its own size into dispersed stable fragments. The successive steps are as follows:

(i) The drop crushes on the impactor and feeds a radially developing sheet of radius $R(t)$, first expanding, then recoiling within a characteristic time τ independent

of the impact Weber number. The asymmetric dynamics of $R(t)$ expresses a simple balance between inertia (that of the initial drop) and capillary restoring forces at the rim (through Culick's law), with the damping term originating from the continuous transfer of momentum from the sheet to the rim. This idealization relies on the particular choice made for the sheets thickness $h(r, t)$ in (3.5), which leads to a very precise agreement for the trajectory $R(t)$ with experiments involving no adjustable parameter. Other choices which also lead to a closed form for $R(t)$ are possible, and among them is the case of a sheet thickness $h(t)$ constant along the radial location r and dependent on time only. That case leads to a symmetrical motion for $R(t)$ not completely inconsistent with the data but less satisfactory than the one corresponding to (3.5) (see Appendix A).

(ii) The expansion and recoil dynamics is essentially made at constant pressure in the liquid. Although its rim is decelerating for most of its development period ($\ddot{R}(t) < 0$), a global Rayleigh–Taylor instability of the expanding sheet is unlikely. However, since the rim sits in a decelerating frame, an associated body force proportional to $-\rho\ddot{R}$ pushes the fluid particles constitutive of the rim radially outward. That force, which originates in the non-Galilean character of the rim motion, induces a Rayleigh–Taylor-like mechanism, localized at the rim. It is at the origin of the radially expelled ligaments, whose breakup ultimately built the overall spray. The corresponding discussion has distinguished between mode selection and radial expulsion, which are two different phenomena. They both occur around wavelengths having the same scaling on We (see (4.15)), but the rate at which the ligaments are expelled is set by the rim deceleration, which is independent of the impacting velocity, as figure 8 demonstrates.

(iii) The final fragment drop size distribution $P(d)$ is a compound of drops coming from the breakup of ligaments themselves distributed in size. The composition rule is the linear superposition in (5.4) of gamma distributions characteristic of ligament breakup $p(d/a)$, weighed by the relative proportion $q(a/\langle d \rangle)$ of the ligaments' initial size a in the toroidal sheet rim of average size $\langle d \rangle$. It generically leads to the family of Bessel function in (5.7) whose shape, typical of fragmentation phenomena in uncontrolled condition such as impacts, is intermediate between a pure power law and an exponential one.

Since the fragmentation of a macroscopic liquid volume mandatorily involves the formation of ligaments as transient objects mediating the subsequent formation of smaller drops, the chronology of events and principles we have evidenced here are generic of drop fragmentation in a general frame. They are likely to also hold beyond the small target limit, as for the more familiar case of a drop impacting a pre-wetted or dry surface.

Appendix A. Expansion dynamics for $h(t)$

For a sheet thickness $h(t)$ dependent solely on time t, one has $u(r, t) = -(\dot{h}/2h)(r - r_0)$ from (3.3), and from the mass balance in (3.7) and dynamical closure at the
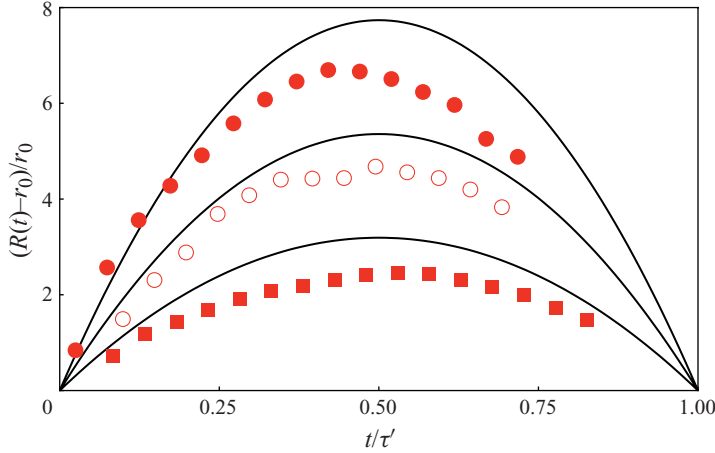
FIGURE 13. (Colour online) Sheet radius evolution as a function of dimensionless time t/τ' for three different impact Weber numbers, $We = 489$ (■), 1378 (○) and 2873 (●), superimposed with the trajectory expected from (A 4). Compare with figure 6, where the fit by (3.16) is more satisfactory.

rim in (3.11), one has, in place of (3.13),

$$h(t)[R(t) - r_0]^2 = \frac{\Omega}{\pi} \left(1 - \frac{t}{\tau'}\right)^2 \quad \text{with} \quad \tau' = \sqrt{\frac{\rho \, \Omega}{2\pi\sigma}}. \qquad (A\,1)$$

Using (3.2) within the same isobaric approximation as the one leading to (3.15), one gets instead

$$\ddot{R} + \frac{2}{(\tau' - t)^2} (R - r_0) + \frac{2}{\tau' - t} \dot{R} = 0 \qquad (A\,2)$$

whose solution is now

$$\frac{R(t) - r_0}{r_0} = \sqrt{\frac{We}{3}} \frac{t}{\tau'} \left(1 - \frac{t}{\tau'}\right), \qquad (A\,3)$$

describing this time a symmetric one-period oscillatory motion lasting for

$$\tau' = \sqrt{\frac{\rho \, d_0^3}{12\sigma}}. \qquad (A\,4)$$

The motion within the sheet $u(r, t)$ and its thickness $h(t)$ is now expected to be

$$u(r, t) = \frac{r}{t}, \quad h(t) \sim \frac{\Omega}{(u_0 t)^2}, \qquad (A\,5)$$

displaying the same scaling dependencies as the ones derived by Yarin & Weiss (1995). As seen in figure 13, that case leads to a symmetrical motion for $R(t)$ not completely inconsistent with the data, with however a somewhat-too-short time period τ' and an overexpected maximal radius.

Appendix B. Pressure in the rim and energy loss

Consider an abrupt expansion in a Galilean frame, like the one in figure 14, and an element of mass $m = \rho u_1 A_1 \Delta t$ passing though the expanding region and being

FIGURE 14. An abrupt expansion from a section A_1 with velocity u_1 to a section A_2 with velocity u_2 accompanied by turbulence and vortices, as imagined by Leonardo Da Vinci (1508).

decelerated from u_1 to u_2 in a time interval Δt. The force needed for the deceleration of this conserved element of mass is

$$f = \frac{\Delta}{\Delta t}(m\,u) = \rho u_1 A_1 \Delta u, \tag{B 1}$$

where $\Delta u = u_2 - u_1$. The force f is equal to the pressure difference $p_1 - p_2$ applied to the section A_2 bordering the mass volume, giving

$$p_2 - p_1 = \rho u_2(u_1 - u_2), \tag{B 2}$$

owing to mass conservation $u_1 A_1 = u_2 A_2$ (Batchelor 1967). The associated loss of energy per unit volume $\dot{w}$ such that

$$\tfrac{1}{2}\rho u_1^2 + p_1 = \tfrac{1}{2}\rho u_2^2 + p_2 + \dot{w} \tag{B 3}$$

is equal, p_1 and p_2 being linked by (B 2) to the kinetic energy of the *velocity loss*

$$\dot{w} = \tfrac{1}{2}\rho(u_1 - u_2)^2, \tag{B 4}$$

a result known since Borda (1763).

If applied to a rim bordering a plane steady liquid sheet of thickness h, the above result permits the inference of the rim velocity v. Fluid particles passing from the sheet to the (much thicker) rim expand and, if the expansion is abrupt enough, dissipate energy according to (B 4) as $\dot{w} = (1/2)\rho v^2$ per unit volume. When the rim has travelled a distance ℓ and has therefore collected a mass $m = \rho h \ell$, the work of capillary forces $2\sigma \ell$ is the kinetic energy of m plus the energy dissipated $\dot{w}\ell h$. Thus

$$2\sigma\ell = \tfrac{1}{2}m\,v^2 + \dot{w}\ell h, \tag{B 5}$$

that is

$$v^2 = \frac{2\sigma}{\rho h}, \tag{B 6}$$

consistent with Taylor (1959) and Culick (1960) who have solved the problem of the receding rim after attempts by Dupré (1867) and Lord Rayleigh (1891), using a flawed version of (B 5) and omitting the dissipation term (see also de Gennes 1996).

If applied to a moving sheet bordered by a stationary rim, as for Savart sheets, the result of (B 4) is also consistent with the observation that fluid particles leave the rim with no remnant kinetic energy, which is fully dissipated on the rim (see e.g. Taylor 1959; Clanet & Villermaux 2002; Bremond *et al.* 2007).

The analogy with the abrupt expansion permits one not only to reformulate Culick's law but also, considering (B 2), to infer that if the fluid is arrested in the rim ($u_2 = 0$) and if the incident knietic energy is dissipated according to (B 4), the pressure difference $p_2 - p_1$ is zero. The numerics in Savva & Bush (2009) tend to support this result. This conclusion holds in a Galilean frame, in the absence of external body forces.

REFERENCES

Abramowitz, M. & Stegun, I. A. 1964 *Handbook of Mathematical Functions*. Dover.

Allen, R. F. 1975 The role of surface tension in splashing. *J. Colloid. Interface Sci.* **51** (2), 350–351.

Ashgriz, N. & Poo, Y. L. 1990 Coalescence and separation in binary collisions of liquid drops. *J. Fluid Mech.* **221**, 183–204.

Bartolo, D., Josserand, C. & Bonn, D. 2005 Retraction dynamics of aqueous drops upon impact on non-wetting surfaces. *J. Fluid Mech.* **545**, 329–338.

Batchelor, G. K. 1967 *An Introduction to Fluid Dynamics*. Cambridge University Press.

Borda, J. C. 1763 Experiences sur la Résistance des Fluides. Mémoires de l'Academie Royale des Sciences, Paris, pp. 356–376.

Bremond, N., Clanet, C. & Villermaux, E. 2007 Atomization of undulated liquid sheets. *J. Fluid Mech.* **585**, 421–456.

Bremond, N. & Villermaux, E. 2005 Bursting thin liquid films. *J. Fluid Mech.* **524**, 121–130.

Bremond, N. & Villermaux, E. 2006 Atomization by jet impact. *J. Fluid Mech.* **549**, 273–306.

Chandra, S. & Avedisian, C. T. 1991 On the collision of a droplet with a solid surface. *Proc. R. Soc. Lond.* A **432**, 13–41.

Clanet, C. & Villermaux, E. 2002 Life of a smooth liquid sheet. *J. Fluid Mech.* **462**, 307–340.

Cossali, G. E., Coghe, A. & Marengo, M. 1997 The impact of a single drop on a wetted solid surface. *Exp. Fluids* **22**, 463–472.

Culick, F. E. C. 1960 Comments on a ruptured soap film. *J. Appl. Phys.* **31**, 1128–1129.

Dupré, A. 1867 Théorie mécanique de la chaleur. *Ann. Chim. Phys.* **11**, 194–216.

Eggers, J. & Villermaux, E. 2008 Physics of liquid jets. *Rep. Prog. Phys.* **71**, 036601.

de Gennes, P. G. 1996 Mechanics of soft interfaces. *Faraday Discuss.* **104**, 1–8.

Kim, H. Y., Feng, Z. C. & Chun, J. H. 2000 Instability of a liquid jet emerging from a droplet collision with a solid surface. *Phys. Fluids* **12** (3), 531–541.

Krechetnikov, R. 2010 Stability of liquid sheet edges. *Phys. Fluids* **22**, 092101.

Lord Rayleigh 1891 Some applications of photography. *Nature* **XLIV**, 249–254.

Marmanis, H. & Thoroddsen, S. T. 1996 Scaling of the fingering pattern of an impacting drop. *Phys. Fluids* **8** (6), 1344–1346.

Marmottant, P. & Villermaux, E. 2004 On spray formation. *J. Fluid Mech.* **498**, 73–112.

Mehdizadeh, N. Z., Chandra, S. & Mostaghimi, J. 2004 Formation of fingers around the edges of a drop hitting a metal plate with high velocity. *J. Fluid Mech.* **510**, 353–373.

Mundo, C., Sommerfeld, M. & Tropea, C. 1995 Droplet–wall collisions: experimental studies of the deformation and breakup process. *Intl J. Multiph. Flow* **21** (2), 151–173.

Pepper, R. E., Courbin, L. & Stone, H. A. 2008 Splashing on elastic membranes: the importance of early-time dynamics. *Phys. Fluids* **20** (8), 082103.

Qian, J. & Law, C. 1997 Regimes of coalescence and separation in droplet collision. *J. Fluid Mech.* **331**, 59–80.

Richard, D., Clanet, C. & Quéré, D. 2002 Contact time of a bouncing drop. *Nature* **417**, 811.

Roisman, I. V., Horvat, K. & Tropea, C. 2006 Spray impact: rim transverse instability initiating fingering and splash, and description of a secondary spray. *Phys. Fluids* **18**, 102104.

Roisman, I. V., Riobo, R. & Tropea, C. 2002 Normal impact of a liquid drop on a dry surface: model for spreading and recedind. *Proc. R. Soc. Lond.* A **458**, 1411–1430.

Rozhkov, A., Prunet-Foch, B. & Vignes-Adler, M. 2002 Impact of water drops on small targets. *Phys. Fluids* **14** (10), 3485–3501.

Rozhkov, A., Prunet-Foch, B. & Vignes-Adler, M. 2003 Impact of drops of polymer solutions on small targets. *Phys. Fluids* **15** (7), 2006–2019.

ROZHKOV, A., PRUNET-FOCH, B. & VIGNES-ADLER, M. 2004 Dynamics of a liquid lamella resulting from the impact of a water drop on a small target. *Proc. R. Soc. Lond.* A **460**, 2681–2704.

SAVART, F. 1833 Mémoire sur le choc d'une veine liquide lancée sur un plan circulaire. *Ann. Chim.* **54**, 56–87.

SAVVA, N. & BUSH, J. W. M. 2009 Viscous sheet retraction. *J. Fluid Mech.* **626**, 211–240.

SIMPKINS, P. G. & BALES, E. L. 1972 Water drop response to sudden accelerations. *J. Fluid Mech.* **55** (4), 629–639.

SQUIRE, H. B. 1953 Investigation of the stability of a moving liquid film. *Br. J. Appl. Phys.* **4**, 167–169.

STERN, S. A., WEAVER, H. A., STEFFL, A. J., MUTCHLER, M. J., MERLINE, W. J., BUIE, M. W., YOUNG, E. F., YOUNG, L. A. & SPENCER, J. R. 2006 A giant impact origin for Pluto's small moons and satellite multiplicity in the Kuiper belt. *Nature* **439**, 946–948.

STOW, C. D. & STAINER, R. 1977 The physical products of a splashing water drop. *J. Met. Soc. Japan* **55** (5), 518–531.

TAYLOR, G. I. 1959 The dynamics of thin sheets of fluid. Part III. Disintegration of fluid sheets. *Proc. R. Soc. Lond.* **253**, 313–321.

TAYLOR, G. I. 1961 A study of the behavior of a thin sheet of a moving liquid. *J. Fluid Mech.* **10**, 305.

THORODDSEN, S., ETOH, T. & TAKEHARA, K. 2006 Crown-breakup by Marangoni instability. *J. Fluid Mech.* **557**, 63–72.

THORODDSEN, S. & SAKAKIBARA, J. 1998 Evolution of the fingering pattern of an impacting drop. *Phys. Fluids* **10** (6), 1359–1374.

TOMOTIKA, S. 1936 Breaking up of drop of viscous liquid immersed in another fluid which is extending at uniform rate. *Proc. R. Soc Lond.* A **153**, 302–318.

TROUTON, F. T. 1906 On the coefficient of viscous traction and its relation to that of viscosity. *Proc. R. Soc. Lond.* **77**, 426–440.

TSIOLKOVSKY, K. E. 1903 The exploration of cosmic space by means of reaction devices. *Rev. Sci. Phil. Lit.* **5**, 1–23.

UKIWE, C. & KWOK, D. Y. 2005 On the maximum spreading diameter of impacting droplets on well-prepared solid surfaces. *Langmuir* **21**, 666–673.

VILLERMAUX, E. 2007 Fragmentation. *Annu. Rev. Fluid Mech.* **39**, 419–446.

VILLERMAUX, E. & BOSSA, B. 2009 Single drop fragmentation determines size distribution of raindrops. *Nature Phys.* **5**, 697–702.

VILLERMAUX, E. & CLANET, C. 2002 Life of a flapping liquid sheet. *J. Fluid Mech.* **462**, 341–363.

DA VINCI, L. 1508 Codex Leicester. In *The Notebooks of Leonardo da Vinci* (ed. and trans. E. MacCurdy). George Brazillier.

WATCHERS, L. H. J. & WESTERLING, N. A. J. 1966 The heat transfer from a hot wall to impinging water drops in the spheroidal sate. *Chem. Engng Sci.* **21**, 1047–1056.

WORTHINGTON, A. M. 1908 *A Study of Splashes*. Longmans, Green.

XU, L., BARCOS, L. & NAGEL, S. R. 2007 Splashing of liquids: interplay of surrounding gas and surface roughness. *Phys. Rev.* E **76**, 066311.

YARIN, A. L. 2006 Drop impact dynamics: splashing, spreading, receding, bouncing . . . . *Annu. Rev. Fluid Mech.* **38**, 159–192.

YARIN, A. L. & WEISS, D. A. 1995 Impact of drops on solid surfaces: self-similar capillary waves, and splashing as a new type of kinematic discontinuity. *J. Fluid Mech.* **283**, 141–173.